

# Minimum reinforcement in concrete structures and material/structural instability

Giuseppe Ferro · Alberto Carpinteri · Giulio Ventura

Received: 15 February 2007 / Accepted: 2 November 2007 / Published online: 18 December 2007  
© Springer Science+Business Media B.V. 2007

**Abstract** The problem of the assessment of minimum reinforcement in concrete members has been examined both theoretically and experimentally by the bridged crack model. The model has been demonstrated to be an efficient numerical tool for investigating the behavior of structural elements in bending, and allowed to show the minimum reinforcement percentage depends on the structural element size, and decreases with increasing beam depths. In the model, Linear Elastic Fracture Mechanics concepts are used to determine the equilibrium and the compatibility equations of a beam segment subjected to bending in presence of a mode I crack. Recently, the model has been extended to include the presence of closing stresses as a function of the crack opening in addition to steel reinforcement closing traction. This allows to characterize the mechanical behavior of fiber reinforced structural elements. A criterion for accounting for crushing in compression has been introduced as well, to bound from below (minimum reinforcement) and from above (maximum reinforcement) a region of stable and ductile mechanical behavior as a function of the mechanical properties as well as of the size of the structural element. Some experimental results are commented under this light.

**Keywords** Minimum reinforcement · Scale effects · Reinforced concrete beams · Transitional failure

phenomena · Brittleness number · Fiber reinforced concrete · Concrete crushing

## 1 Introduction

In recent years an increasing interest has been concentrated on high performance concretes and on the possibility to ameliorate the mechanical properties of traditional reinforcement with dispersed fibers. While sometimes these additions try to solve problems like fire resistance, durability and impact or vibrations resistance, there are many noticeable applications where their role is mainly structural, in the aim to replace or reduce traditional steel bar reinforcement. These aspects require the development of computational models suitable to describe their mechanical properties. In particular, the mechanical interaction of fibers added to the concrete matrix is to be accounted for, extending the analysis beyond a qualitative assertion of improved crack toughness of the matrix.

The bridged crack model for RC beams was introduced by (Carpinteri 1981a,b, 1984) and it was proficiently used for the determination of the size dependent minimum reinforcement in concrete members (Bosco et al. 1990, 1992; Bosco and Carpinteri 1992a,b, 1995). The model was reformulated in (Carpinteri and Massabó 1997a,b, Carpinteri and Massabó 1996) for unreinforced concrete members with cohesive closing stresses and extended to the simultaneous presence of both steel and fibers in (Carpinteri et al. 2003). The ability of

G. Ferro (✉) · A. Carpinteri · G. Ventura  
Department of Structural and Geotechnical Engineering,  
Politecnico di Torino, 10129 Torino, Italy

dealing at the same time with steel reinforcements and closing stresses in the matrix results in a very flexible model, capable of modeling a wide range of concrete materials. Moreover, while limit state analysis yields only the ultimate load, the bridged crack model reveals in addition scale effects, instability phenomena and brittle–ductile transition of the structural element, because of its Fracture Mechanics foundations.

The general problem has been addressed in literature by several authors with different approaches, like finite element numerical analysis by Hillerborg et al. (1976), linear elastic Fracture Mechanics models (Baluch et al. 1992), cohesive crack models (Hawkins and Hjørsetet 1992; Ruiz 2001). One of the main differences between the models is the way the steel bar reinforcement transfers the stresses to the concrete matrix. The influence of this element into the global behavior of the models when simulating experimental results is not clear yet. As an example Ruiz (2001), by comparing to experimental results reported in (Ruiz et al. 1998), found that the bond-slip taking place between the concrete and the reinforcement plays a central role in determining the peak load. However, as pointed out by the Author, this result was found for lightly reinforced beams, below the minimum fixed by design codes for structural members, otherwise the load–displacement curve may differ significantly (Ruiz 2001). A general analysis for modeling the complete macroscopic response of fiber reinforced concrete is presented in (Karihaloo and Wang 2000), while (Karihaloo 1995) illustrates Fracture Mechanics in the light of its application to concrete.

In the bridged crack model the bar traction is considered applied on the crack faces, and a rigid-plastic constitutive law for the bar is employed. Moreover, the traction is spread over the reinforcement to eliminate the singularity arising from the application of concentrated forces. The problem of accounting for a limit to

the compressive stresses in concrete is considered. This is formulated as an upper limit to the value of the brittleness number characterizing the bridged crack model. In the paper two different approaches are presented: in the first this limit is established by limit state analysis and is restricted to absence of cohesive stresses; in the second the concept of nondimensional maximum compressive stress is introduced, and influence functions are determined based on LEFM models. The latter method allows accounting for cohesive stresses distributed on the crack edges, and is therefore able to assess the influence of fibers in concrete crushing collapse.

The model is analyzed showing the influence of the nondimensional parameters on the mechanical response for ordinary steel bar reinforcement, fiber reinforcement and mixed bar and fiber reinforcement. A size dependent minimum reinforcement is observed in all of the three cases, and the mechanical behavior itself is shown to depend on the element size, exhibiting different brittle–ductile transitions.

Some experimental results are finally simulated and commented.

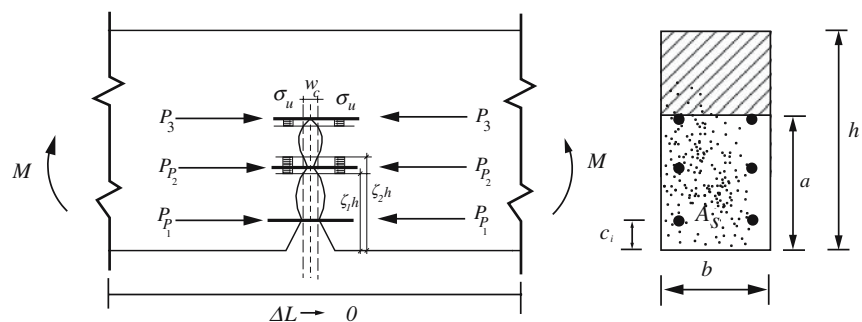
## 2 Modeling reinforced beams by Fracture Mechanics

### 2.1 The bridged crack model

In this section the model is briefly recalled. More details can be found in the references cited in Sect. 1. A scheme of the model is reported in Fig. 1, with some of the used symbols.

The distribution of the discrete forces  $P_i$  and the continuous ones  $\sigma$  applied to the crack surfaces represent the bridging mechanism of the steel bars and cohesive stresses, respectively. The nondimensional position of the  $i$ -th steel reinforcement is denoted by  $\zeta_i = c_i/h$ ,

**Fig. 1** Model scheme of a cracked beam cross section



while  $\sigma(w)$  represents the constitutive relation of the cohesive and/or fiber traction,  $w$  being the crack opening at a generic point along the crack. Function  $\sigma(w)$  is assumed to be zero for  $w$  greater than a critical value  $w_c$ . Its actual expression can be derived from experimental results or model codes and can be assumed to represent an homogenized constitutive law for both the closing stresses due to the cohesion of plain concrete and the bridging action of the fibers. Its simplest expression can be one of the following power laws

$$\frac{\sigma}{\sigma_u} = 1 - \left(\frac{w}{w_c}\right)^n; \quad \frac{\sigma}{\sigma_u} = \left(\frac{w}{w_c}\right)^n \tag{1}$$

characterized by the maximum traction  $\sigma_u$ , by the critical crack opening displacement  $w_c$  and by the exponent  $n$ . Other laws may be used to represent at the same time the matrix and the fiber toughening action, e.g. bilinear laws (Carpinteri and Massabó 1996).

The constitutive relation for the reinforcement bars is assumed as rigid-plastic with no upper limit to the maximum deformation.

The maxima for the bridging actions are defined by the ultimate traction  $P_{P_i} = A_i \sigma_y$  for the bars and by the ultimate stress  $\sigma_0 = \gamma \sigma_u$  for the fibers (or matrix),  $A_i$  being the  $i$ -th bar area,  $\gamma$  the effective volumetric percentage of fibers,  $\sigma_y$  and  $\sigma_u$  the minimum between yielding and sliding stress for the bars and fibers, respectively. By effective volumetric percentage of fibers it is meant that the volumetric percentage should be reduced to account for the random orientation and distribution of fibers. As a matter of fact, the product  $\gamma \sigma_u$  should be equal to the apparent ultimate concrete traction stress including the presence of fibers.

With reference to Fig. 1, let  $K_I$  be the stress intensity factor at the crack tip. By the superposition principle, it is given by the sum of the stress intensity factors  $K_{IM}$  due to the bending moment,  $K_{Ii}$  due to the  $m$  reinforcement bar traction  $P_i$  and  $K_{I\sigma}$  due to the distributed closing stresses  $\sigma(w)$  along the crack (Carpinteri et al. 2003; Ferro 2002):

$$\hat{K}_{IC} = K_{IM} - \sum_{i=1}^m K_{Ii} - K_{I\sigma} \tag{2}$$

where  $\hat{K}_{IC}$  is given by:

$$\hat{K}_{IC} = \begin{cases} K_{IC} & \text{bridging option} \\ 0 & \text{cohesive option} \end{cases} \tag{3}$$

Therefore, in the bridging option, the crack propagation condition is ruled by the comparison of the stress

intensity factor  $K_I$  to the matrix toughness  $K_{IC}$ . On the other hand, in the cohesive option, the stress intensity factor is assumed to be zero at the fictitious crack tip (Carpinteri and Massabó 1997a,b, 1996). The value of  $K_{IC}$  in (2) may be determined by the RILEM recommendations (RILEM TC50 1985; RILEM TC89 1990), or derived by the procedures suggested in (Abdalla and Karihaloo 2003; Karihaloo et al. 2003).

The stress intensity factors can be expressed in the form (Carpinteri and Massabó 1997a):

$$K_{IM} = \frac{M_F}{bh^{1.5}} Y_M(\xi) \tag{4}$$

$$K_{Ii} = \frac{P_i}{bh^{0.5}} Y_P(\xi, z_i) \tag{5}$$

$$K_{I\sigma} = \sum_{i=1}^{n_c} \frac{1}{bh^{0.5}} \int_{\zeta_{1i}}^{\zeta_{2i}} \sigma(w(\zeta)) Y_P(\xi, \zeta) bh \, d\zeta. \tag{6}$$

In (6)  $n_c$  is the number of cohesive zones, where  $\sigma(w) \neq 0$ . These zones are defined over the intervals  $[\zeta_{1i}, \zeta_{2i}]$ ,  $i = 1 \dots n_c$ .

Let  $\rho = A_s/bh$  be the bar reinforcement percentage and define the brittleness numbers  $N_P^{(1)}$ ,  $N_P^{(2)}$  and the nondimensional critical crack opening for the cohesive stresses  $\tilde{w}_c$  as:

$$N_P^{(1)} = \rho \frac{\sigma_y h^{1/2}}{K_{IC}}; \quad N_P^{(2)} = \gamma \frac{\sigma_u h^{1/2}}{K_{IC}}; \quad \tilde{w}_c = \frac{E w_c}{K_{IC} h^{1/2}}. \tag{7}$$

Substituting (5) and (6) in (2), the following nondimensional equilibrium equation is obtained:

$$\tilde{M}_F = \frac{1}{Y_M(\xi)} \left( \frac{\hat{K}_{IC}}{K_{IC}} + N_P^{(1)} \sum_{i=1}^m \tilde{\rho}_i \tilde{P}_i Y_P(\xi, z_i) + N_P^{(2)} \sum_{i=1}^{n_c} \int_{\zeta_{1i}}^{\zeta_{2i}} \tilde{\sigma}(\tilde{w}) Y_P(\xi, \zeta) \, d\zeta \right) \tag{8}$$

where:

$$\tilde{M}_F = \frac{M_F}{K_{IC} b h^{1.5}}; \quad \tilde{P}_i = \frac{P_i}{P_{P_i}}; \quad \tilde{\rho}_i = \frac{\rho_i}{\rho}; \quad \tilde{\sigma} = \frac{\sigma(w(\zeta))}{\gamma \sigma_u}. \tag{9}$$

The equilibrium Eq. (8) gives the bending crack propagation moment as a function of the bar traction and of the closing stresses. These quantities depend on the crack opening profile by means of the constitutive equations.

The crack opening at a general nondimensional abscissa  $\zeta$  can be determined by adding the three contributions of the bending moment, bar traction and closing

stresses. The nondimensional opening, evaluated at the crack propagation bending moment  $M = M_F$ , has the following expression:

$$\begin{aligned} \tilde{w} = & \tilde{w}_M - \tilde{w}_P - \tilde{w}_\sigma = 2\tilde{M}_F \int_{\zeta}^{\xi} Y_M(x) Y_P(x, \zeta) dx + \\ & - 2N_P^{(1)} \sum_{i=1}^m \tilde{\rho}_i \tilde{P}_i \int_{\max(\zeta, \zeta_i)}^{\xi} Y_P(x, z_i) Y_P(x, \zeta) dx + \\ & - 2N_P^{(2)} \sum_{i=1}^{n_c} \int_{h_1(\zeta)}^{\xi} \int_{\zeta_{1i}}^{h_2(x)} \tilde{\sigma} Y_P(h_2(x), y) dy \\ & \times Y_P(x, \zeta) dx \end{aligned} \tag{10}$$

where:

$$h_1(\zeta) = \max(\zeta, \zeta_{1i}); \quad h_2(x) = \min(x, \zeta_{2i}). \tag{11}$$

By introducing the rigid-plastic constitutive equation for the bars, the displacement evaluated at  $\zeta = \zeta_i$ ,  $i = 1 \dots m$  equals zero if  $P_{P_i} - P_i < 0$ , i.e. if  $1 - \tilde{P}_i < 0$ . Then, let  $H$  be the Heaviside step-function. The diagonal matrix  $[H_P] = \text{diag} \left( H(1 - \tilde{P}_i) \right)$ ,  $i = 1 \dots m$ , allows for expressing the vector of the openings at the reinforcement bars as:

$$\{\tilde{w}\} = [H_P] \left( \{\tilde{\lambda}_M\} \tilde{M} - [\tilde{\lambda}] \{\tilde{P}\} - \{\tilde{w}_\sigma\} \right) \tag{12}$$

where the elements of the above vectors and matrices are  $(i, j = 1 \dots m)$ :

$$\{\tilde{\lambda}_M\}_i = 2 \int_{z_i}^{\xi} Y_M(x) Y_P(x, z_i) dx \tag{13}$$

$$[\tilde{\lambda}]_{ij} = 2N_P^{(1)} \tilde{\rho}_j \int_{\max(z_i, z_j)}^{\xi} Y_P(x, z_i) Y_P(x, z_j) dx \tag{14}$$

$$\{\tilde{w}_\sigma\}_i = \tilde{w}_\sigma(z_i). \tag{15}$$

The inverse relation to (12), giving  $\{\tilde{P}\}$  as a function of  $\{\tilde{w}\}$  is:

$$\begin{aligned} \{\tilde{P}\}_i &= \begin{cases} ([\tilde{\lambda}]^{-1} (\{\tilde{\lambda}_M\} \tilde{M} - \{\tilde{w}\} - \{\tilde{w}_\sigma\}))_i & \tilde{w}_i = 0 \\ 1 & \tilde{w}_i > 0 \end{cases} \quad i = 1 \dots m \end{aligned} \tag{16}$$

Equation (12), with  $\tilde{M}$  given by (8), is a nonlinear integral equation in the unknowns  $\tilde{w}$ ,  $n_c$ ,  $[\zeta_{1i}, \zeta_{2i}]$ ,  $i = 1 \dots n_c$ . Its solution for a fixed crack depth  $\xi$  allows for the determination of the opening function, the crack propagation bending moment  $\tilde{M}_F$  through (8) and the relative rotation of the cross section, given in nondimensional form by:

$$\begin{aligned} \tilde{\phi} = & \phi \frac{Eh^{0.5}}{K_{IC}} = \tilde{\phi}_M - \sum_{i=1}^m \tilde{\phi}_I - \tilde{\phi}_\sigma \\ = & 2\tilde{M}_F \int_0^{\xi} Y_M^2(\zeta) d\zeta \\ & - 2N_P^{(1)} \sum_{i=1}^m \tilde{\rho}_i \tilde{P}_i \int_{z_i}^{\xi} Y_P(\zeta, z_i) Y_M(\zeta) d\zeta \\ & - 2N_P^{(2)} \sum_{i=1}^{n_c} \int_{\zeta_{1i}}^{\xi} \int_{\zeta_{1i}}^{h_2(x)} \tilde{\sigma} Y_P(h_2(x), y) \\ & dy Y_M(x) dx, \end{aligned} \tag{17}$$

with  $h_2(x)$  given by (11).

### 3 Elimination of singularities

It has been observed (Carpinteri and Massabó 1997a,b) that the singularity of the function  $Y_P$  implies the compliance (14) to diverge when  $i = j$ , i.e. the integral defining the compliance  $\lambda_{ii}$

$$\lambda_{ii} = \frac{2}{Eb} \int_{z_i}^{\xi} Y_P(x, z_i) Y_P(x, z_i) dx \tag{18}$$

is improper. From a physical point of view, this is a consequence of accounting for a concentrated force which is, as a matter of fact, absent. To solve this issue, suppose that the traction at the reinforcement is spread over a zone of height  $d_i$  (so that the area of the reinforcement  $A_{s_i}$  is equal to  $d_i b$ ), and let  $\tilde{d}_i = d_i / h$ . The compliance  $\lambda_{i p_i}$  representing the crack opening displacement at the fiber level  $\zeta_i$  due to a unit traction distribution  $p_i = 1$  over the height  $d_i$ , is given by

$$\lambda_{i p_i} = \frac{2}{Eb} \frac{1}{\tilde{d}_i} \int_{\zeta_i}^{\xi} \int_{\zeta_i - \tilde{d}_i/2}^{\min(y, \zeta_i + \tilde{d}_i/2)} Y_P(y, \zeta) d\zeta Y_P(y, \zeta_i) dy \tag{19}$$

An offset  $\delta_i$  of the lower integration limit, termed *cutoff* (Carpinteri and Massabó 1997a,b), is introduced so that  $\lambda_{i p_i} = \lambda_{ii}$

$$\begin{aligned} & \int_{z_i}^{\xi} Y_P(x, z_i) Y_P(x, z_i) dx \\ &= \frac{1}{\tilde{d}_i} \int_{\zeta_i}^{\xi} \int_{\zeta_i - \tilde{d}_i/2}^{\min(y, \zeta_i + \tilde{d}_i/2)} Y_P(y, \zeta) d\zeta Y_P(y, \zeta_i) dy \end{aligned} \tag{20}$$

The above equation is solved on  $\delta_i$  as a function of  $\tilde{d}_i$ . Note that it is

$$\tilde{d}_i = \frac{d_i}{h} = \frac{b d_i}{bh} = \frac{A_{s_i}}{A} = \rho_i \tag{21}$$

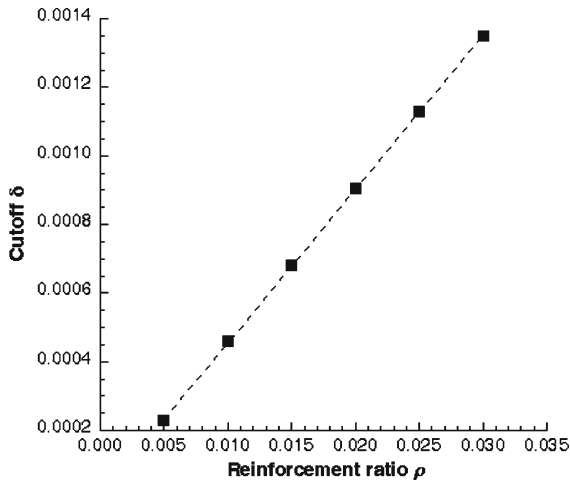


**Fig. 2** Computed cutoff values (full squares) and linear fit of the data (dashed line)

i.e.  $\tilde{d}_i$  has the physical meaning of the reinforcement ratio  $\rho_i$ . This assumption is confirmed when modelling experimental tests.

Note that, when solving (20), the cutoff is observed being basically independent of the crack depth  $\xi$  and the reinforcement position  $\zeta_i$ . Consequently, a single reinforcement is considered and the values  $\xi = 0.5$ ,  $\zeta_1 = 0.1$  are assumed. The computed nondimensional cutoff  $\delta$  for some typical values of the reinforcement ratio are plotted in Fig. 2 and reported in Table 1. The cutoff values can be conveniently expressed through the law:

$$\delta = 9 \times 10^{-6} + 0.044771 \rho \tag{22}$$

### 4 Concrete crushing and maximum reinforcement

#### 4.1 Limit state analysis

The bridged crack model described so far does not include any criterion for accounting for the strength of the concrete in compression. This limit can be introduced by limit state analysis (CEB-FIB model) and is restricted to absence of cohesive stresses.

In the limit state analysis model, crushing of concrete in bending is attained when the deformation

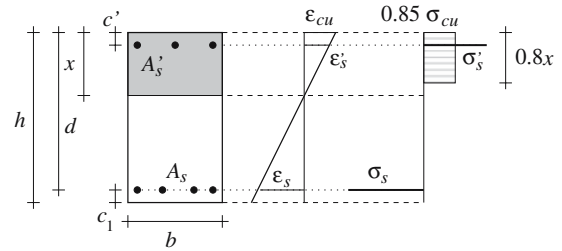


**Fig. 3** CEB-FIB simplified model for a rectangular section in bending

reaches the critical value  $\epsilon_{cu} = 0.0035$ . Concrete is simulated by a nonlinear law, which may be simplified assuming a rectangular stress block in compression, whose height is  $0.8d$ ,  $d$  being the distance of the neutral axis from the upper edge of the rectangular section. The maximum compressive stress in concrete is given in this model by  $0.85\sigma_{cu}$ , where  $\sigma_{cu}$  is the compressive strength. This is illustrated in Fig. 3, where all the quantities used in the present derivation are defined as well.

With reference to Fig. 3, the following equations hold:

– linear deformation field

$$\epsilon_s = \frac{d - x}{x} \epsilon_{cu} \tag{23}$$

– equilibrium (rotation and translation)

$$M = b \cdot 0.8 x \cdot 0.85 \sigma_{cu} (d - 0.4x) - \sigma_s \eta A_s (d - c') \tag{24}$$

$$\sigma_s A_s = b \cdot 0.85 \sigma_{cu} \cdot 0.8x + \sigma_s \eta A_s \tag{25}$$

where  $\eta = \frac{A'_s}{A_s}$ . The steel bars are assumed with linear elastic behavior up to the yielding stress  $\sigma_y$ , when the strain  $\epsilon_y$  is reached. Then, perfectly plastic behavior up to the rupture strain  $\epsilon_{su}$  is assumed (usually  $\epsilon_{su} = 0.01$ ).

Some observations allow for a solution of the above equations in closed form. First of all, as the strain in concrete is fixed to the crushing value, the problem has solution only for a tension reinforcement area greater

**Table 1** Values of the cutoff  $\delta$  as a function of the reinforcement ratio  $\rho$

$\rho$ (%)	0.1	0.5	1.0	1.5	2.0	2.5	3.0
$\delta$	0.0000538	0.00023	0.00046	0.00068	0.000905	0.00113	0.00135

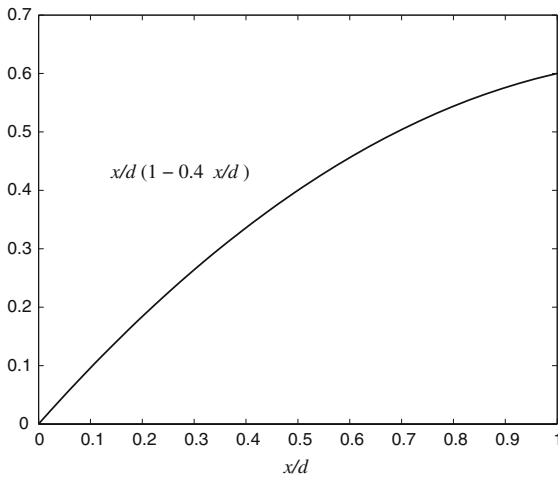


**Fig. 4** Trend of the bending moment curve as a function of the nondimensional neutral axis position

than a minimum value  $A_{sc}$  to be determined. Moreover for any  $A_s > A_{sc}$  a different value of the bending moment  $M$  at crushing is obtained. A qualitative plot of the bending moment as a function of the neutral axis position is sketched in Fig. 4: it is observed a monotonically increasing function of the position  $x$ . As a consequence, because of the equilibrium, the bending moment at concrete crushing is a monotonically increasing function of the tension reinforcement area  $A_s$ . When  $x \rightarrow d$ ,  $A_s \rightarrow \infty$  while the reinforcement stress decreases to zero.

The minimum bending moment producing the crushing collapse of concrete is therefore obtained when the maximum allowable strain  $\epsilon_{yu}$  in the tension reinforcement is present. This condition is assumed here, being both a safe and optimal design condition at the same time.

It will be therefore assumed  $A_s = A_{sc}$ . The value of  $A_{sc}$  can be computed by the condition that the deformation and stress in the tension steel are the rupture ones, i.e.  $\epsilon_s = \epsilon_{su}$ ,  $\sigma_s = \sigma_y$ . From (23) the neutral axis position is determined as:

$$x = \frac{\epsilon_{cu}}{\epsilon_{su} - \epsilon_{cu}} h, \tag{26}$$

and, upon substitution of the usual values for the maximum strains, it is obtained

$$x = 0.259 h \tag{27}$$

A final consideration holds for the stresses in the compression reinforcement steel. It is observed that for

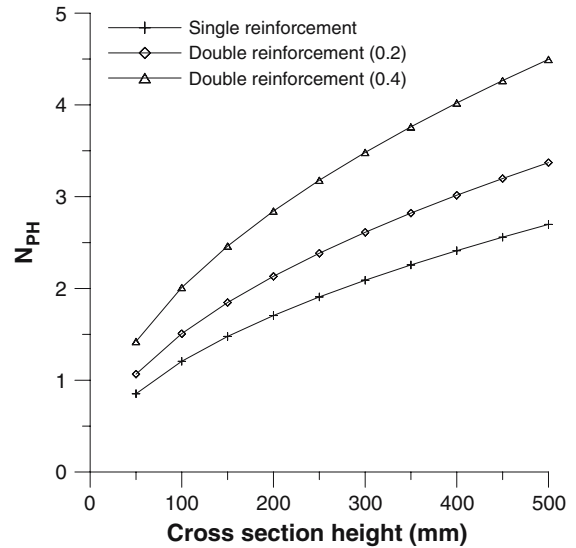


**Fig. 5** Maximum brittleness number for single and double reinforced beams

usual beam geometries ( $c' \ll h$ ) and steel type, the compression reinforcement yields significantly before concrete crushing, so that  $\sigma'_s = \sigma_y$  can be assumed.

The minimum reinforcement area inducing concrete crushing failure is obtained after substitution of (27) into (25)

$$A_{sc} = \frac{0.176}{1 - \eta} b d \frac{\sigma_{cu}}{\sigma_y}; \quad \eta < 1. \tag{28}$$

From this equation, observing that  $h = d + c_1$  and dividing by  $bh$  both terms, the critical reinforcement area ratio  $\rho_{sc}$  is obtained, and upon substitution into the brittleness number definition it follows:

$$N_{PH}^{(1)} = 0.176 \frac{1 - \zeta_1}{1 - \eta} \frac{\sigma_{cu} h^{0.5}}{K_{IC}}; \quad \eta < 1. \tag{29}$$

In Fig. 5 a plot of  $N_{PH}^{(1)}$  is reported assuming the data  $\sigma_{cu} = 48.2 \text{ Nmm}^{-2}$ ,  $K_{IC} = 63.4 \text{ Nmm}^{-3/2}$ ,  $\zeta_1 = 0.1$ ,  $\eta = 0.1, 0.2, 0.4$ , by varying the cross section height in between 50 and 500 mm.

The value  $N_{PH}^{(1)}$  defines the upper limit of applicability for the bridged crack model both for beams with single or double reinforcement. Beams having  $N_P^{(1)} > N_{PH}^{(1)}$  will exhibit failure by concrete crushing.

On the other hand, the model allows for the determination of the minimum reinforcement so that the rupture is ductile. This has been determined experimentally in (Bosco and Carpinteri 1992a,b), where the Authors introduced the following relation between the

minimum brittleness number  $N_{PC}^{(1)}$  and the mean compressive strength of concrete:

$$N_{PC}^{(1)} = 0.1 + 0.0023\sigma_{cu} \tag{30}$$

$\sigma_{cu}$  being expressed as  $N/mm^2$ . A beam having a brittleness number lower than the limit expressed by (30) exhibits a brittle failure because of insufficient reinforcement. In this case, when the crack develops at the lower edge and crosses the reinforcement, it is immediately yielded and strained to rupture, so that the peak load is higher than the yielding branch. This concept will be detailed in Sect. 5.

Consequently, a region of brittleness number values where a beam has ductile behavior is naturally defined:

$$N_{PC}^{(1)} < N_P^{(1)} < N_{PH}^{(1)} \tag{31}$$

#### 4.2 Determining concrete crushing by Fracture Mechanics

While in the former section concrete crushing has been determined through limit state analysis, here this phenomenon is analyzed by Fracture Mechanics concepts leading to a formal development more coherent with the bridged crack model. The basic concept is to express the stress state at the upper edge of the cracked section as the sum of the contribution due to the bending moment and the one of the forces acting on the crack edges

$$\sigma_c = \sigma_c^M + \sum_{i=1}^m \sigma_c^{Pi} + \sigma_c^\sigma \tag{32}$$

Note explicitly that, although (32) is formally similar to (2), the stress given by (32) is computed at the uppermost edge of the beam, not at the crack tip. Therefore, in the present approach, the compressive stress is assumed to be increasing above the crack tip with its maximum at the top edge. Concrete crushing will be detected by comparing this stress to a maximum *admissible* value. It is known (Hillerborg 1990) that, when concrete is close to crushing, the stress block may present its maximum between the crack tip and the top edge. This effect is not included in the present model. On the other hand, this collapse mechanism is usually to be avoided in real applications because of the brittleness of the structural collapse.

By introducing two new nondimensional functions  $Y_\sigma^M$  and  $Y_\sigma^P$ , the above contributions can be written as:

$$\sigma_c^M = \frac{M}{bh^2} Y_\sigma^M(\xi) \tag{33a}$$

$$\sigma_c^{Pi} = \frac{P_i}{bh} Y_\sigma^P(\xi, \zeta_i) \tag{33b}$$

$$\sigma_c^\sigma = \frac{1}{bh} \int \sigma Y_\sigma^P dA = \frac{1}{h} \int_0^a \sigma(w) Y_\sigma^P d\zeta \tag{33c}$$

To rewrite Eqs. (33) in nondimensional form, the definition of brittleness numbers, nondimensional bending moment  $M = \tilde{M} K_{IC} bh^{3/2}$  and traction  $P_i = \tilde{P}_i bh\sigma_y\rho_i$  are considered, and being:

$$\frac{P_i}{bh} = \frac{\tilde{P}_i bh\sigma_y\rho_i}{bh} N_P^{(1)} \frac{K_{IC}}{\rho\sigma_y h^{0.5}} = N_P^{(1)} \frac{K_{IC}}{h^{0.5}} \frac{\rho_i}{\rho} \tilde{P}_i \tag{34}$$

$$\begin{aligned} \frac{\sigma}{bh} &= N_P^{(2)} \frac{K_{IC}}{\gamma\sigma_u h^{0.5}} \frac{\sigma}{bh} = N_P^{(2)} \frac{K_{IC}}{bh^{1.5}} \frac{\sigma}{\gamma\sigma_u} \\ &= N_P^{(2)} \frac{K_{IC}}{bh^{1.5}} \tilde{\sigma}, \end{aligned} \tag{35}$$

it follows that:

$$\sigma_c^M = \frac{K_{IC}}{h^{0.5}} Y_\sigma^M(\xi) \tilde{M} \tag{36}$$

$$\sigma_c^{Pi} = \frac{K_{IC}}{h^{0.5}} N_P^{(1)} \frac{\rho_i}{\rho} Y_\sigma^P(\xi, \zeta_i) \tilde{P}_i \tag{37}$$

$$\sigma_c^\sigma = N_P^{(2)} \frac{K_{IC}}{h^{1.5}} \int_0^a \tilde{\sigma}(w) Y_\sigma^P d\zeta \tag{38}$$

and, introducing the change of variables  $y = \zeta h$  in (38) and extending the integral where the cohesive traction is nonzero:

$$\sigma_c^\sigma = N_P^{(2)} \frac{K_{IC}}{h^{1.5}} \int_0^\xi \tilde{\sigma}(w(\zeta)) Y_\sigma^P(\xi, \zeta) h d\zeta \tag{39}$$

$$= N_P^{(2)} \frac{K_{IC}}{h^{0.5}} \sum_{i=1}^{n_c} \int_{\zeta_{1i}}^{\zeta_{2i}} \tilde{\sigma}(w(\zeta)) Y_\sigma^P(\xi, \zeta) d\zeta \tag{40}$$

Consequently, the following nondimensional stresses  $\tilde{\sigma}_c$  are defined:

$$\tilde{\sigma}_c^M = Y_\sigma^M(\xi) \tilde{M} \tag{41}$$

$$\tilde{\sigma}_c^{Pi} = N_P^{(1)} Y_\sigma^P(\xi, \zeta_i) \tilde{P}_i \tag{42}$$

$$\tilde{\sigma}_c^\sigma = N_P^{(2)} \sum_{i=1}^{n_c} \int_{\zeta_{1i}}^{\zeta_{2i}} \tilde{\sigma}(w(\zeta)) Y_\sigma^P(\xi, \zeta) d\zeta \tag{43}$$

and Eq. (32) can be expressed in non dimensional form:

$$\tilde{\sigma}_c = \tilde{\sigma}_c^M + \sum_{i=1}^m \tilde{\sigma}_c^{Pi} + \tilde{\sigma}_c^\sigma \tag{44}$$

so that:

$$\sigma_c = \frac{K_{IC}}{h^{0.5}} \left[ \tilde{\sigma}_c^M + \sum_{i=1}^m \tilde{\sigma}_c^{P_i} + \tilde{\sigma}_c^\sigma \right] \tag{45}$$

The determination of functions  $Y_\sigma^M$  and  $Y_\sigma^P$  may be carried out numerically. A cracked beam segment has been considered, subjected to a bending moment at the ends or to a force along the crack edges. In these two configurations, the stress  $\sigma_c$  has been evaluated by adaptive finite elements analysis using standard plane stress elements, Fig. 6. The two following functions have been obtained by a nonlinear regression of the data

$$Y_\sigma^M(\xi) = -5.997 + 3.269\xi - \frac{5.400\xi}{(1-\xi)^2} - 16.311\xi^2 - 3.721\xi^3 \tag{46}$$

$$Y_\sigma^P(\xi, \zeta) = \frac{\xi - \zeta}{(1-\xi)^2} \left( -10.286 + 10.959\xi - 6.112\xi^2 - 9.574\zeta + 13.509\xi\zeta - 3.835\zeta^2 \right) \tag{47}$$

Other, more precise functions, may be determined using quarter points elements and/or changing the basis adopted for the nonlinear regression.

The above development allows for evaluating the maximum compressive stress in the concrete considering the effect of closing stresses distributed on the crack faces. This result cannot be obtained with the traditional analysis showed in the previous section. A plot of the nondimensional stress, Eq. (44), versus the crack depth  $\xi$  is shown in Fig. 7. For the sake of comparison to the experimental results presented in the following, the Figure refers to the case where no distributed closing stresses are present, i.e.  $N_p^{(2)} = 0$ ,  $N_p = N_p^{(1)} \neq 0$ . The curves present a slope discontinuity when yielding of the reinforcing bars occurs. In the following section it will be shown how the upper limit  $N_{pH}$ , Eq. (31), can be derived from Fig. 7 with reference to experimental results.

### 5 Response of the model to the variation of the nondimensional parameters and scale effects

In the present section it will be shown how the values of the brittleness numbers  $N_p^{(1)}$  and  $N_p^{(2)}$  as well as the nondimensional critical crack opening  $\tilde{w}_c$  affect

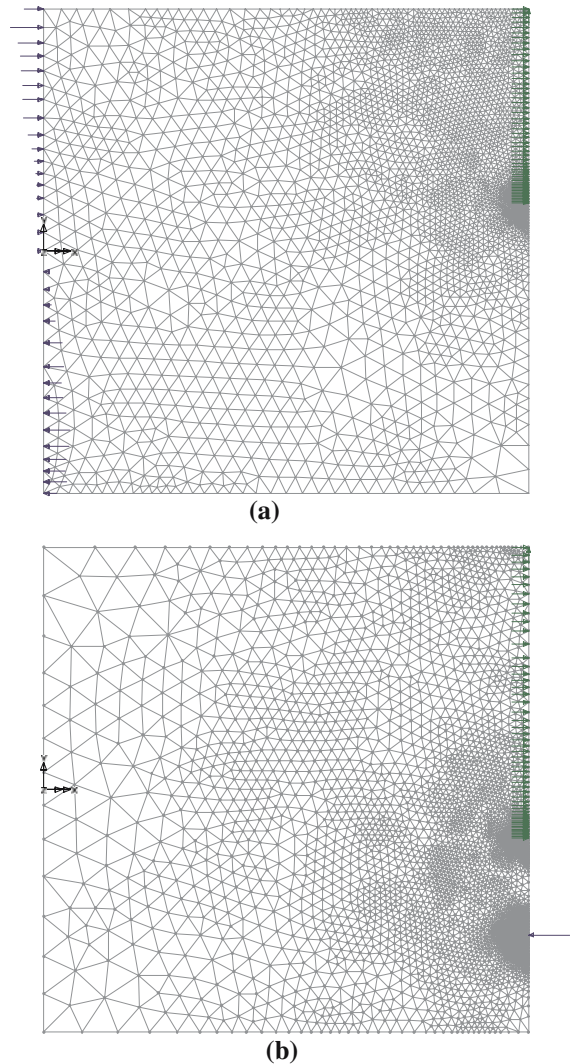


**Fig. 6** Two F.E. models used for the evaluation of (a)  $\sigma_c^M$  and (b)  $\sigma_c^P$ . The short, uniform arrows, represent the constraints along the symmetry axis

the mechanical response of the beam and imply scale effects. Results will be given for the two simple cases where only steel bars or cohesive stresses are present, as well as in the coupled case where both bars and fibers coexist.

#### 5.1 Steel bar reinforcements

A single reinforcement placed at  $\zeta_1 = 0.1$  is considered, with cutoff  $\delta = 0.00046$ . The nondimensional bending moment is plotted as a function of the crack

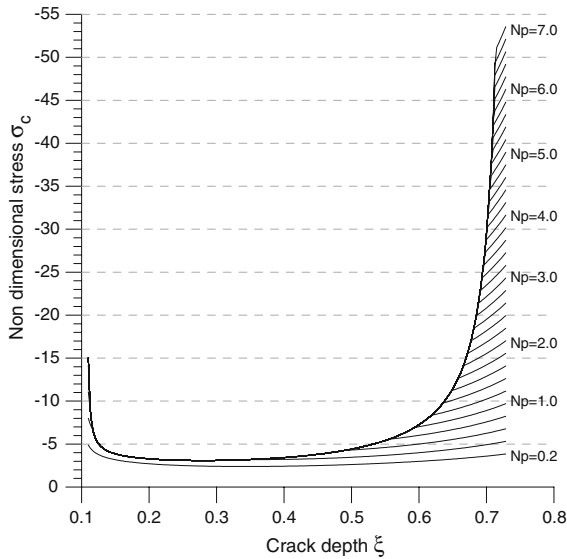


**Fig. 7** Nondimensional maximum compressive stress in the upper part of the cross section as a function of the crack depth  $\xi$

depth in Fig. 8. The Figure refers to four values of the brittleness number  $N_p^{(1)}$ , from 0.1 to 2.0. In this case, only the bridging option will be considered. Due to the singularity represented by the steel bar, a sharp discontinuity is present at  $\xi = \zeta_1$ , so that the graphs are influenced by the steel reinforcement percentage for  $\xi > \zeta$ . When  $\xi > \zeta$ , depending on the value of  $N_p^{(1)}$ , the curves may be monotonically decreasing (e.g.  $N_p^{(1)} = 0.1$  in Fig. 8) or present a minimum point after which the bending moment is increasing as the crack depth increases. For very low brittleness numbers this minimum does not exist evidencing a completely unstable response of the beam because of insufficient minimum reinforcement, while for higher brittleness numbers the existence of the minimum point implies a stable response of the beam. An experimental determination of the brittleness number  $N_{pC}^{(1)}$  separating the two behavior classes and defining the minimum reinforcement is given in Eq. (30). Because of the definition of the brittleness number (7), proportional to  $\sqrt{h}$ , a scale effect is evidenced, so that the minimum reinforcement percentage decreases with the square root of the beam height.

When yielding of the bar occurs the graph shows a slope discontinuity, and the sign of the slope of the curve after yielding evidences stable or unstable behavior. The bending moment at yielding is assumed as the

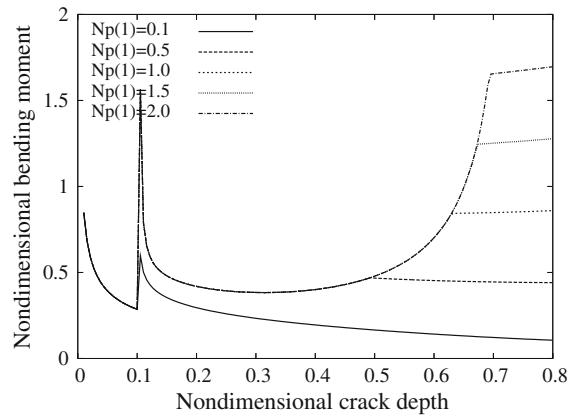


**Fig. 8** Nondimensional bending moment as a function of the crack depth  $\xi$

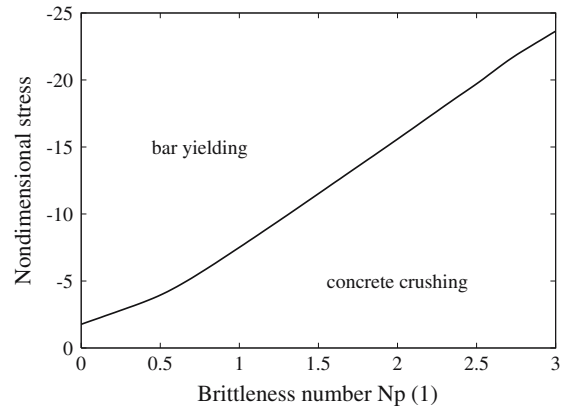


**Fig. 9** Nondimensional compressive stress vs.  $N_p^{(1)}$

failure load for the beam, in the hypothesis no concrete crushing takes place up to this point.

To know whether bar yielding or concrete crushing takes place, the plot of the brittleness number versus the compressive stress  $\sigma_c$  at bar yielding is considered, Fig. 9. If, for a given brittleness number, the value of  $\sigma_c$  reported in the graph is greater than the one allowable for the material, then concrete crushing precedes bar yielding, and the collapse will be brittle. In this sense, Fig. 9 represents a collapse mode map.

### 5.2 Fiber reinforcement

When only fiber or concrete matrix cohesive stresses are present, only the brittleness number  $N_p^{(2)}$  is nonzero. Assuming a rigid-plastic constitutive law for the fibers,

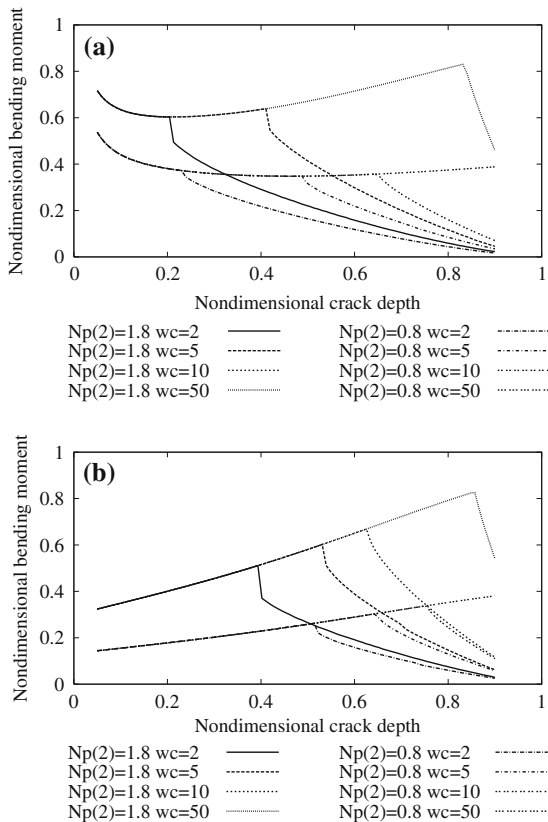


**Fig. 10** Nondimensional bending moment as a function of the crack depth  $\xi$  by varying the brittleness number  $N_p^{(2)}$  and the nondimensional critical opening. (a) bridging option, (b) cohesive option

the nondimensional critical opening  $\tilde{w}_c$  rules the extension and evolution of the cohesive zone, Fig. 10.

While in the bridging option the curves present a singularity for a vanishing crack depth, in the cohesive option the bending moment starts from a finite value, as expected. Because of the assumed constitutive law for the fibers, the bending moment increases as the crack depth increases, until the crack opening reaches the critical value at the farthest point from the crack tip. Then a moment drop follows due to the vanishing action of the fibers where the critical opening has been exceeded. This phenomenon occurs for higher crack depths in the cohesive option due to the different condition assumed at the crack tip (3).

In particular, it should be noted how an higher value of the brittleness number  $N_p^{(2)}$  directly increases the resistance by translating upwards the curve, while the nondimensional critical opening influences the peak

bending moment and the crack depth from which the unstable branch starts. This justifies the use of long crimped fibers for structural purposes.

The nondimensional parameters  $N_p^{(2)}$  and  $\tilde{w}_c$  controlling the mechanical response can be related when the toughness  $K_{IC}$  is referred to the homogenized composite. With this assumption  $K_{IC} = \sqrt{E} \mathcal{G}_F$ ,

$$\mathcal{G}_F = \int_0^{w_c} \sigma(w) dw \tag{48}$$

being the fracture energy. Consequently (Carpinteri and Massabó 1997a,b), the fracture energy does not depend on the crack profile and is equal to  $\alpha \gamma \sigma_u w_c$ , where  $\alpha$  is a constant depending on the shape of the bridging law.

Moreover, the products

$$N_p^{(1)} \tilde{w}_c = \frac{\rho \sigma_y h^{0.5}}{K_{IC}} \frac{E w_c}{K_{IC} h^{0.5}} = \frac{\rho \sigma_y E w_c}{K_{IC}^2} = \frac{\rho \sigma_y w_c}{\mathcal{G}_F}, \tag{49}$$

$$N_p^{(2)} \tilde{w}_c = \frac{\gamma \sigma_u h^{0.5}}{K_{IC}} \frac{E w_c}{K_{IC} h^{0.5}} = \frac{\gamma \sigma_u E w_c}{K_{IC}^2} = \frac{\gamma \sigma_u w_c}{\mathcal{G}_F}, \tag{50}$$

do not depend on the height of the cross section. Parametric graphs constructed assuming constant products  $N_p^{(1)} \tilde{w}_c$  and  $N_p^{(2)} \tilde{w}_c$  are therefore independent of the size of the structural element.

### 5.2.1 Cohesive option and scale effects

If the cohesive option is assumed and  $N_p^{(1)} = 0$ , the plots of  $\tilde{M}$  vs.  $\tilde{\phi}$  and  $\tilde{M}$  vs. the crack depth  $\xi$  are given in Fig. 11 for a constant product  $N_p^{(2)} \tilde{w}_c = 36$ .

The plots are computed by varying  $\xi$  in the interval  $\xi \in (0, 0.9]$ . The curves are monotonically increasing until the critical crack opening is reached at the farthest point from the tip. Then the bridging zone rapidly reduces as well as the bending moment: small-scale bridging condition is determined, and all the curves tend to envelope the LEFM limit curve (Carpinteri and Massabó 1997a,b). Therefore a transition from stable (positive slope) to unstable behavior is predicted by the model after reaching the maximum bending moment.

As shown before, once the mechanical properties of fibers and concrete matrix are fixed, the curves of constant product  $N_p^{(2)} \tilde{w}_c$  represent the change of the beam response as the height of the cross section is varied.

Then, a size effect can be immediately evidenced evaluating the maxima of the curves of Fig. 11. In fact

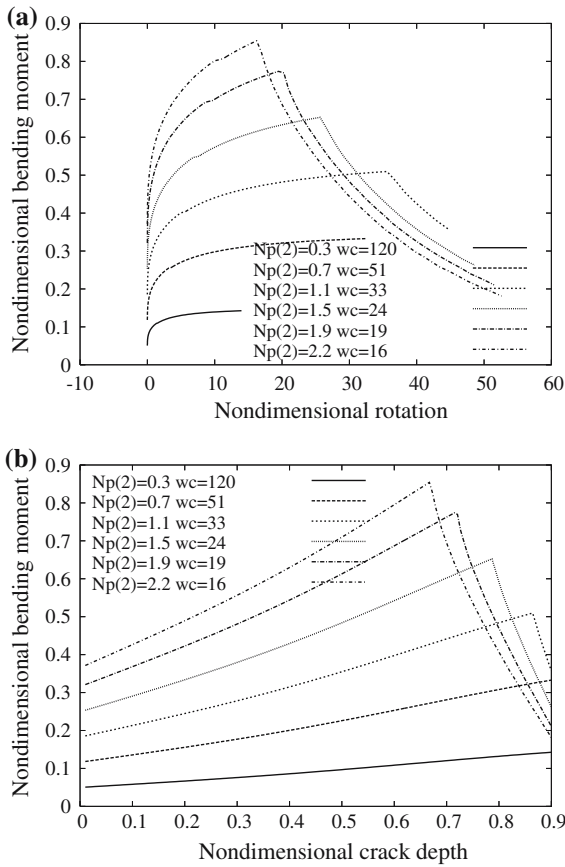


**Fig. 11** Nondimensional bending moment as a function (a) of the crack depth  $\xi$  and (b) of the nondimensional rotation  $\tilde{\phi}$  for a constant product  $N_p^{(2)} \tilde{w}_c = 36$  (cohesive option)

the maxima are observed to increase linearly with  $N_p^{(2)}$ , i.e. the maximum bending moment increases proportionally to  $\sqrt{h}$  whereas, considering the conventional technical theory of the beam, it should be increasing proportionally to  $h^2$ .

5.2.2 Bridging option and scale effects

If the bridging option is assumed and  $N_p^{(1)} = 0$ , the plots of  $\tilde{M}$  vs.  $\tilde{\phi}$  and  $\tilde{M}$  vs. the crack depth  $\xi$  are given in Fig. 12 for a constant product  $N_p^{(2)} \tilde{w}_c = 36$ . The plots are constructed for  $\xi$  in the interval  $\xi \in (0, 0.9]$ .

The bridging option evidences a more complex response compared to the cohesive option. With reference to Fig. 12 the bending moment is at first infinite because of the bridging option assumed for vanishing crack depth. Then, for low values of the brittleness number  $N_p^{(2)}$ , the response is completely unstable (e.g.

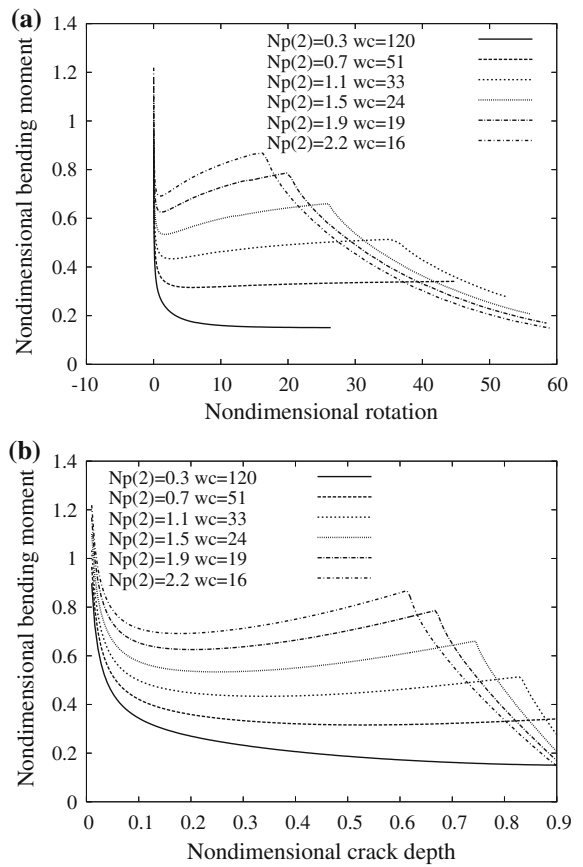


**Fig. 12** Nondimensional bending moment as a function (a) of the crack depth  $\xi$  and (b) of the nondimensional rotation  $\tilde{\phi}$  for a constant product  $N_p^{(2)} \tilde{w}_c = 36$  (bridging option)

$N_p^{(2)} = 0.3$ ). For increasing values of the brittleness number ( $N_p^{(2)} = 0.7$ ) the response becomes stable. Then for higher values ( $N_p^{(2)} > 0.7$ ) a snap-through instability arises, with a stable mechanical behavior until the maximum allowable bending moment is reached. After the maximum, a rapid loss of the load carrying capacity is observed, generating unstable behavior. This is due to the crack opening exceeding the critical value  $w_c$  at the farthest point from the crack tip. The crack opens with a rapid loss of rigidity and a small scale bridging condition is realized, so that the mechanical behavior is basically typical of LEFM, governed only by the matrix toughness  $K_{IC}$ .

As pointed out in the discussion about the cohesive option, the curves in Fig. 12 represent cross sections with the same mechanical properties of fibers and concrete and the same fiber volumetric percentage as the

height of the cross section varies. Consequently, a beam of higher cross section requires a lower fiber percentage to have a stable mechanical response, and a size effect on the minimum volumetric percentage of fibers is predicted.

Finally note that, even if for both the cohesive and the bridging option some curves do not present the descending branch, their final behavior is necessarily brittle either for deeper crack depth than the limit assumed in the computation or because of concrete crushing.

### 5.3 Mixed fiber and bar reinforcement

This is the most interesting case in practical applications. In fact, a calibration of the fiber/bar reinforcement percentages to achieve some particular mechanical behavior of the beam is not trivial without considering very complex simulation tools, e.g. nonlinear finite elements. In Fig. 13 the model has been used to simulate a beam with brittleness numbers  $N_p^{(1)} = 1$  and  $N_p^{(2)} = 1.6$  varying the nondimensional critical opening  $\tilde{w}_c$  between 0 and 100. The case  $\tilde{w}_c = 0$  has been simulated by assuming  $N_p^{(2)} = 0$ . As previously pointed out, in this case only the bridging option can be used, while when  $\tilde{w}_c \neq 0$  both bridging and cohesive option results are plotted.

The plots in Fig. 13 show an increase in the bending moment as the fibers are introduced, as well as a steeper slope of the curves. The nondimensional critical opening controls the crack depth from which the fibers start the debonding process. As the cohesive zone reduces, the curves tend to the one with  $N_p^{(2)} = 0$  (no fibers).

Although the bending moment versus crack depth curves are not monotone, the computed maximum compressive stress can be regarded as an increasing function of the crack depth, for depths sufficiently larger than the reinforcing bar position coordinate, Fig. 14. As in the case where only reinforcing steel bars are present, we may define the maximum allowable bending moment for the cross section as the one for which bar yielding takes place. The value of  $\tilde{\sigma}_c$  computed in this condition is such that, if it is less than the maximum allowable stress for the material, then the collapse will take place by bar yielding; otherwise concrete crushing will occur.

To evaluate the scale effects on the response of fiber and bar reinforced beams, all the mechanical properties

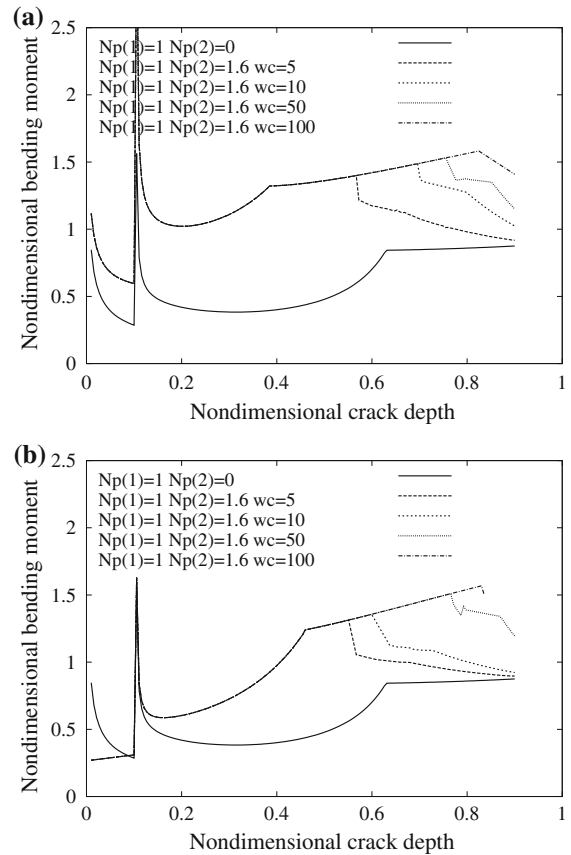


**Fig. 13** Nondimensional bending moment as a function of the crack depth  $\xi$  by varying the nondimensional critical opening. (a) bridging option, (b) cohesive option.

of the materials are fixed as well as the reinforcement percentages. As the height of the beam varies, both  $N_p^{(1)}, N_p^{(2)}$  and  $\tilde{w}_c$  vary but, as pointed out before, their products  $N_p^{(1)}\tilde{w}_c, N_p^{(2)}\tilde{w}_c$  are constant. A family of curves is consequently obtained as  $h$  varies. In Fig. 15 such curves are reported for both the bridging and the cohesive option assuming  $N_p^{(1)}\tilde{w}_c = 61.36$  and  $N_p^{(2)}\tilde{w}_c = 36.00$ .

The plots show that, by varying the height  $h$ , the response is completely unstable (insufficient reinforcements) for low brittleness numbers, e.g.  $N_p^{(1)} = 0.17, N_p^{(2)} = 0.10$  in Fig. 15 then, for increasing brittleness numbers, the unstable branch is followed by a stable (hardening) behavior until an eventual failure by concrete crushing. For larger brittleness numbers a new transition is observed, so that the response is unstable, then stable and finally unstable, see the higher curves in Fig. 15, evidencing a double transition.

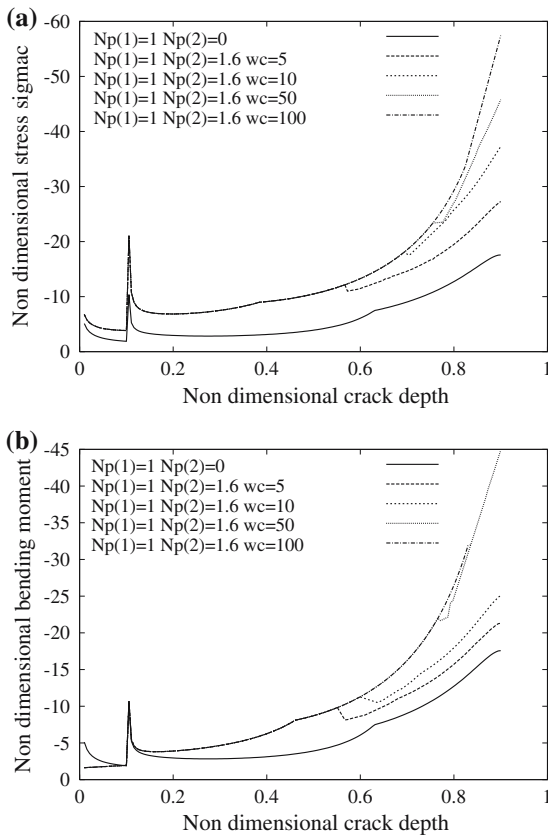


**Fig. 14** Nondimensional stress as a function of the crack depth  $\xi$  by varying the nondimensional critical opening. (a) bridging option, (b) cohesive option

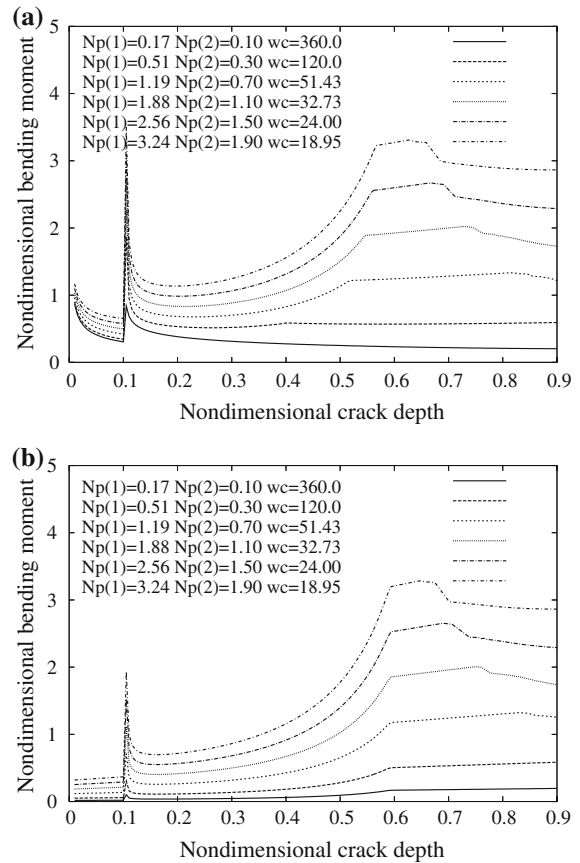


**Fig. 15** Nondimensional bending moment as a function of the crack depth  $\xi$  by varying the nondimensional critical opening, for constant values of the products  $N_p^{(1)} \tilde{w}_c = 61.36$  and  $N_p^{(2)} \tilde{w}_c = 36.00$ . (a) bridging option, (b) cohesive option

## 6 Experimental results

### 6.1 Beams with steel bar reinforcement

The behavior predicted by the inequality (31) has been confirmed by the experimental results provided by Bosco and Carpinteri (Carpinteri et al. 1999). The Authors examine three series of reinforced beams by varying the cross section and the reinforcement area. The tests were performed on 35 beams of classes A, B and C, with cross-sectional area equal to  $100 \times 100$ ,  $100 \times 200$  and  $200 \times 400$  mm, respectively, Fig. 16, and concrete properties  $\sigma_{cu} = 48.2 \text{ Nmm}^{-2}$ ,  $K_{IC} = 63.4 \text{ Nmm}^{-3/2}$ .

The examined reinforcement percentages are 0.12%, 0.25%, 0.50%, 1.00%, 2.00%. The beams are labeled with the letter of the series, the reinforcement percentage and, occasionally, with the slenderness ratio  $L/h$ , e.g. A025-6 means a series A beam with 0.25%

reinforcement and  $L/h = 6$ . In Fig. 17 the brittleness numbers computed for the experimental tests are plotted together with the value of  $N_{PC}$ , Eq. 30, and the curves of  $N_{PH}$  computed by limit state analysis,  $N_{PH}(LS)$ , Eq. 29, and by the bridged crack model,  $N_{PH}(BC)$ . The latter curve,  $N_{PH}(BC)$ , has been derived from Fig. 7. In Fig. 18 the nondimensional maximum stress value, computed with the above material data and cross section heights  $h = 50, 100, 200, 300, 400, 500$  mm, intersects the  $\xi$  vs.  $\tilde{\sigma}_c$  curves. The  $\tilde{\sigma}_c$  curves are drawn for several values of  $N_p^{(1)}$ , and each one presents a slope discontinuity when the steel reinforcement yields. Then, for a given height, the limit condition occurs when at the same time the maximum value of  $\tilde{\sigma}_c$  is attained and the reinforcement yields. The brittleness number in this situation is  $N_{PH}$  and has been determined graphically from the family of curves

**Fig. 16** Geometry of the beams tested by Carpinteri et al. (1999)

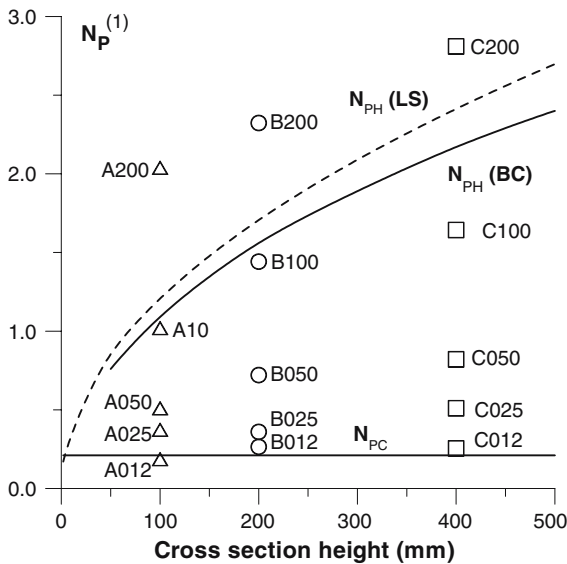
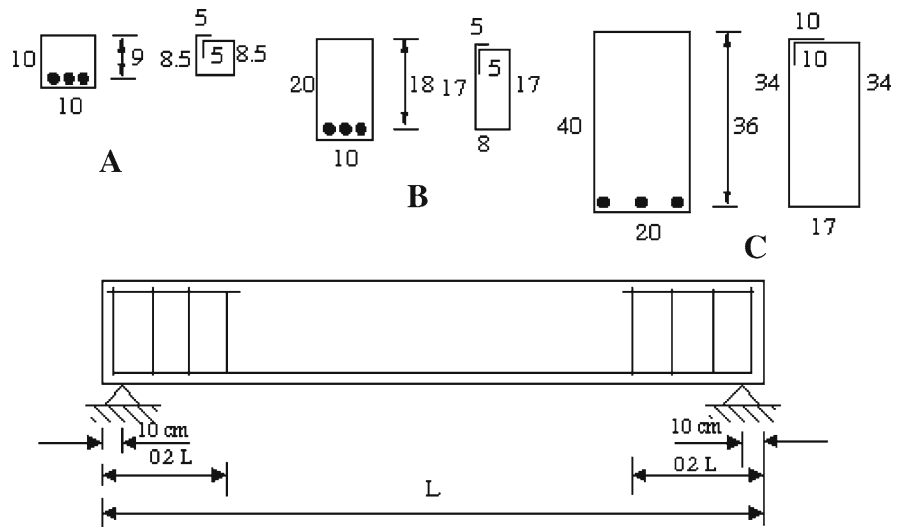


**Fig. 17** Brittleness numbers for the tested beams and curve of the concrete crushing limit  $N_{PH}^{(1)}$

with varying  $N_P^{(1)}$ , Fig. 18. These values are plotted in Fig. 17 as the solid curve  $N_{PH}(BC)$ . The comparison to the limit analysis approach (dashed line) evidences a similar trend, but the Bridged Crack model is able to account for the presence of fibers or cohesion of the matrix and its different dimensional effect.

The experimental results confirm that all the beams above the  $N_{PH}$  curve failed experimentally because of concrete crushing, Fig. 19, while the beams with  $N_P < N_{PC}$  failed for insufficient reinforcement, Fig. 20. All

the above concepts about minimum and maximum reinforcement can be immediately translated into minimum and maximum reinforcement area, the brittleness number  $N_P^{(1)}$  being proportional to this quantity. Equating the definition of  $N_P^{(1)}$  to Eq. (29), considering the data from Fig. 18 and Eq. 30, two curves are determined enclosing the reinforcement percentages for a given section height so that the mechanical behavior is ductile. This is shown in Fig. 21 for both the limit state (LS, dashed curve) and bridged crack (BC, solid curve) approaches. The small oscillations observed in the figure are due to the graphical procedure used to extract the  $N_{PH}$  values from the parametric curves of Fig. 18.

For some beams of the series B and C the load–displacement curves has been simulated by the bridged crack model. The model produces as a result the values of the nondimensional bending moment and rotation as functions of the crack depth. For comparison with the experimental results these values have been converted into displacement versus load diagrams. The conversion is realized by considering the scheme of Fig. 22, where a three point bending test is depicted. The displacement at midspan of the beam is supposed as given by an elastic part plus a rigid part due to the concentrated rotation of the cracked section. From the definition of nondimensional bending moment and rotation, we can write:

$$M_F = \tilde{M} K_{IC} b h^{1.5}, \tag{51}$$

$$\phi = \frac{\tilde{\phi} K_{IC}}{E^* h^{0.5}}. \tag{52}$$

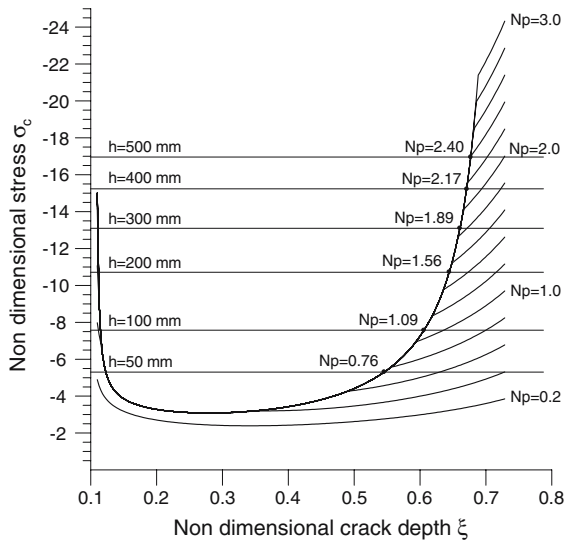


Fig. 18 Determination of the brittleness number  $N_{PH}$

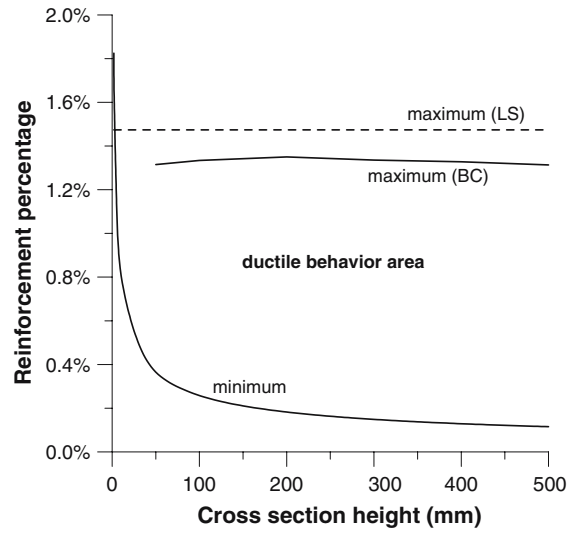


Fig. 21 Reinforcement percentages for ductile cross sections

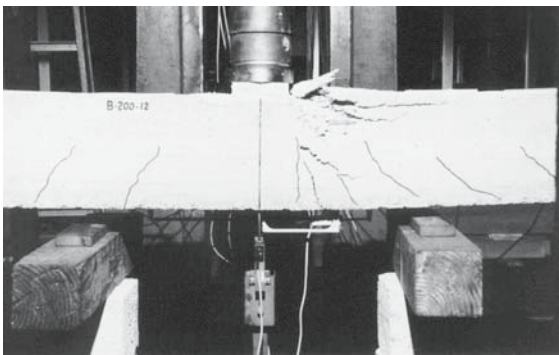


Fig. 19 Brittle failure mode (crushing in compression) of the beam B200

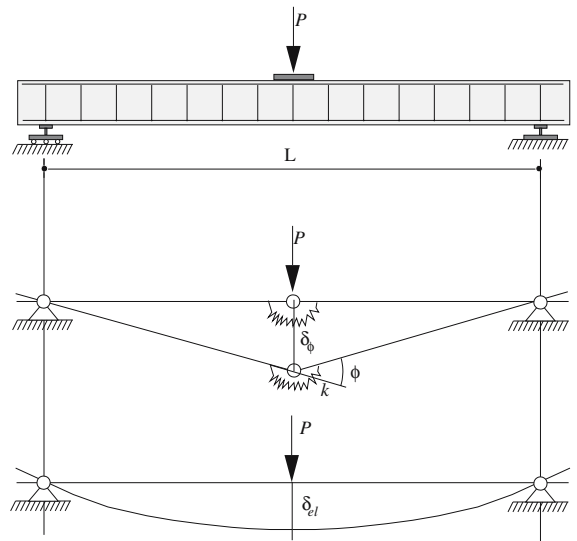


Fig. 22 Details of test beams and plastic hinge formation

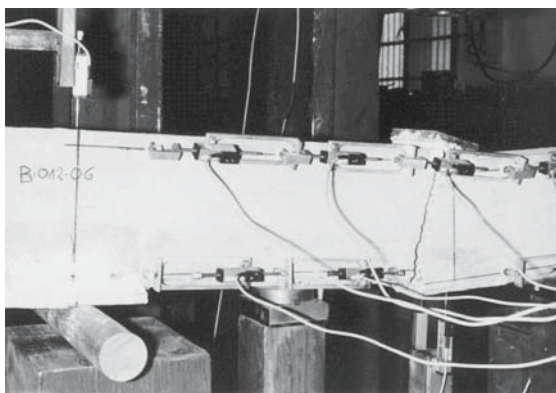


Fig. 20 Brittle failure mode (insufficient reinforcement) of the beam B012

Consequently, the vertical load and displacement at midspan are given by:

$$P = \frac{4M_F}{L}, \tag{53}$$

$$\delta = \delta_{el} + \delta_{\phi} = M_F \frac{L^2}{48E^*I} + \frac{\phi L}{4}, \tag{54}$$

where the inertia is related to the total cross section,  $L$  is the span length, and  $E^* = E/2.2$ ,  $E$  being the conventional 28 days static modulus. This assumption

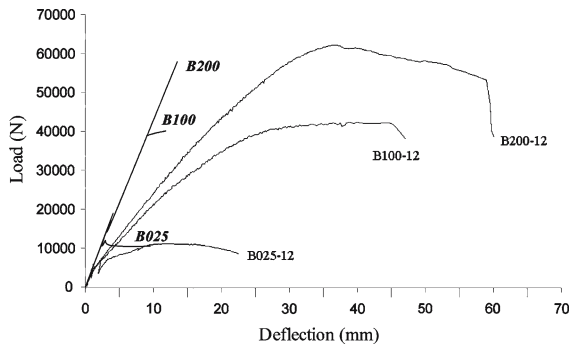


**Fig. 23** Experimental and computed load versus deflection diagrams for the series B12 beams

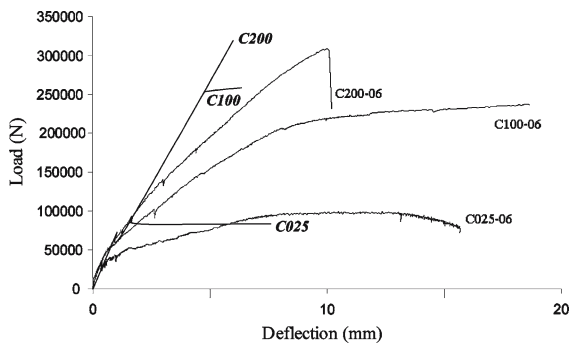


**Fig. 24** Experimental and computed load versus deflection diagrams for the series C6 beams

is known in the literature, e.g. (Carpinteri 1981a,b; Jenq and Shah 1986), and takes into account the nonlinear material behavior in the zone ahead the crack tip.

The experimental and computed load versus deflection diagrams are reported in Figs. 23 and 24. The numerical simulation has been carried out using the bridging option and assuming the data reported in (Carpinteri et al. 1999). The model is of course not able to reproduce the progressive decrease of the tangent modulus due to concrete damage and to the formation of other eventual cracks along the span. This effect is particularly marked in these experimental tests, while much closer results for the load–displacement curves will be shown in the next section. Although the deflection is not closely reproduced, the model is able of simulating the mechanical behavior of the beams, and noticeably the initially unstable behavior of the ones with the lowest reinforcement percentage (B025, C025), the steel yielding collapse of the beams B100 and C100, and the concrete crushing collapse of B200 and C200.

## 6.2 Beams with steel bar and fiber reinforcements

The bridged crack model has been used to simulate some experimental results reported in (Swamy et al. 1981). Two different three point bending tests have been considered, related to beams having the same geometry and tension steel reinforcement. The two tests are denominated DR30 and DR32 in (Swamy et al. 1981) and differ in the fiber volume ratio. The beam DR30 is made by plain concrete and the beam DR32 has 1% fiber volume ratio. The beams have rectangular cross section ( $130 \times 203$  mm) and a total length of 2,500 mm. The distance between the supports is 2,250 mm. The beam is reinforced with  $2 \varnothing 12$  high-strength steel bars (yield strength =  $617 \text{ N/mm}^2$ ). The steel percentage is  $\rho = 0.99\%$  of the cross section area, as reported by the Authors, if the area is computed assuming as height the distance between the bars and the upper side of the cross section (176 mm, see Fig. 1 in (Swamy et al. 1981)). According to the model presented in this paper, the steel percentage is referred to the total cross section area, so that the steel percentage to be considered is  $\rho = 0.86\%$ . For the beam DR30 the reduced elastic modulus  $E^*$  is equal to  $12.786 \text{ KN/mm}^2$ .

Observing the experimental results reported in (Swamy et al. 1981), it has been noticed that the load versus displacement diagram for the beam DR30 must be referred to a tension steel with a resistance higher than the reported one ( $617 \text{ N/mm}^2$ ). In fact, the maximum load corresponds to a bending moment at midspan whose value is higher than the effective height of the cross section times the traction at the steel reinforcement. For this reason a tension steel reinforcement strength equal to  $725 \text{ N/mm}^2$  has been considered in the simulations.

Therefore, for the beam DR30, assuming a matrix toughness  $K_{IC} = 35.76 \text{ N/mm}^{3/2}$ , the brittleness number  $N_p^{(1)}$  is given by:

$$N_p^{(1)} = \frac{\rho \sigma_y \sqrt{h}}{K_{IC}} = 2.484. \quad (55)$$

The experimental and computed load versus displacement diagrams are reported in Fig. 25. The numerical simulation has been carried out using the bridging option, as the fibers were not present in this case. The results of the model do not catch the progressive decrease of the tangent modulus due to concrete damage, although reproduce closely the qualitative behavior

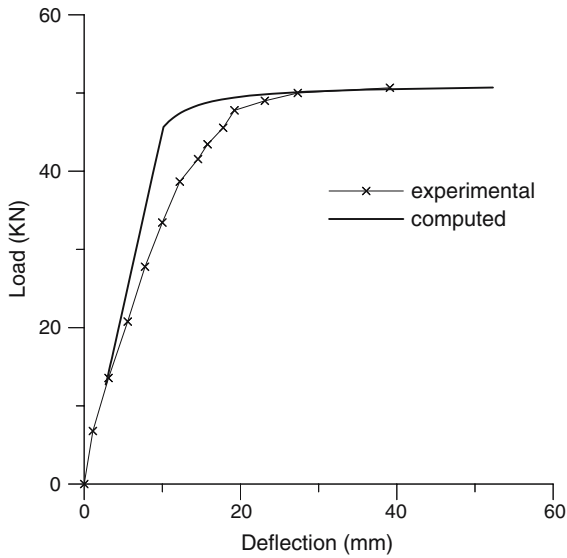


**Fig. 25** Experimental and computed load versus deflection diagrams for the beam DR30

of the structural member as well as the limit load. The latter result is due to assumed steel strength.

The mechanical parameters adopted for the beam DR30, have been used for the simulation of the test DR32, where crimped steel fibers have been added to concrete. The steel fibers are characterized by a length equal to 50 mm, a diameter equal to 0.5 mm, a strength of  $1,050 \text{ N/mm}^2$  and are mixed with concrete with a percentage of 1%.

A first reduction factor of  $1/3$  is to be assumed for the fiber volume percentage, for taking into account the random spatial distribution of the fibers inside the matrix. This simple assumption is based on the observation that the fibers are fully effective if their direction is coaxial with the beam axis, and totally ineffective if they are directed along the other two orthogonal spatial directions. In addition, a further reduction must account for the fact that the fibers are not bisected by the crack, but intersected at a random point along their length (Li et al. 1991). For this reason the “effective density” of the fibers to be introduced in the model has been assumed equal to 0.2%, i.e.  $1/5$  of the real one.

These assumptions provide a brittleness number  $N_P^{(2)}$ :

$$N_P^{(2)} = \frac{\gamma \sigma_u \sqrt{h}}{K_{IC}} = 0.84. \tag{56}$$

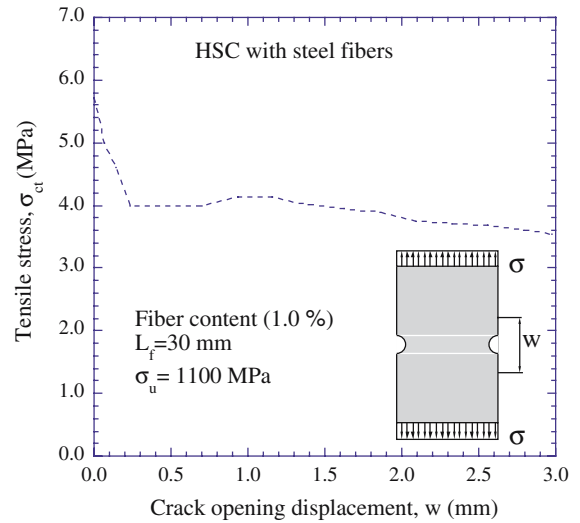


**Fig. 26** Response of high-strength concrete with fibers

Finally, a rigid-perfectly plastic law is considered for the fibers. This assumption finds justification considering experimental results on similar steel fibers (Noghabai 2000), see Fig. 26. As the experimental load versus displacement diagrams have always positive slope with no slope discontinuities, the tension steel does not enter softening behavior and the fibers do not break along the crack depth, i.e., the crack opening is always less than the critical value  $w_c$  and the cohesive zone extends along the whole crack depth. In fact, when the critical opening  $w_c$  is achieved, the load versus displacement diagram exhibits a softening branch, or at least a slope discontinuity. This is compatible with the fibers used in the experiment, as the crack opening at the maximum load is about 5 mm.

Consequently, the data used for running the numerical simulation of the beam DR32 are the two brittleness numbers (55) and (56), the parameter  $\tilde{w}_c$  being not influent ( $\tilde{w} < \tilde{w}_c$ ). Figure 27 reports the experimental load versus displacement graphs compared to the computed ones, in both the cohesive and the bridging option. The two curves are almost coincident, although in the two cases the nondimensional diagram bending moment versus crack depth markedly differs, Fig. 28. As expected, for a given nondimensional moment the crack depth is higher in the cohesive option. In fact, with reference to Fig. 28, once the value  $\tilde{M} = 1$  is fixed, a crack depth  $\xi = 0.4376$  (bridging option) or  $\xi = 0.5446$  (cohesive option) is found.

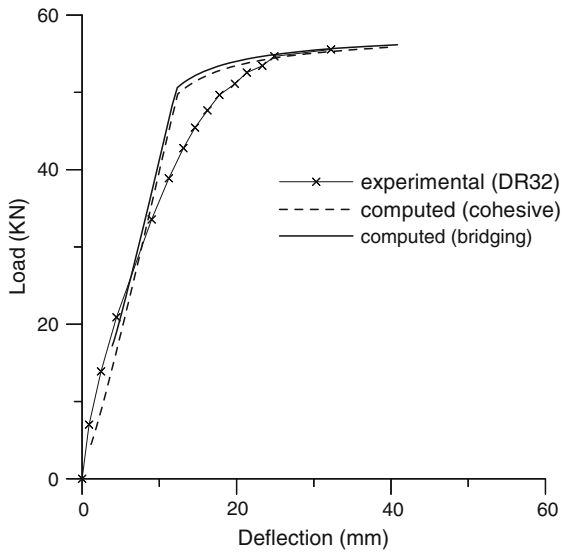


**Fig. 27** Experimental and computed load versus deflection diagrams for the beam DR32

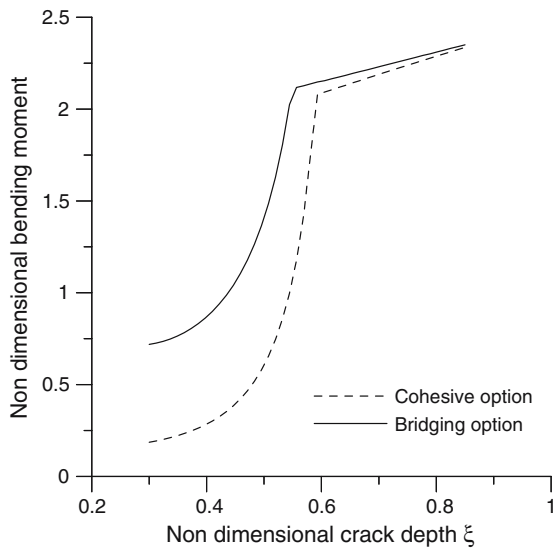


**Fig. 28** Nondimensional bending moment versus crack depth diagrams for the beam DR32

## 7 Conclusions

The bridged crack model has been recently extended to the simultaneous presence of conventional steel bar reinforcement and fibers mixed into the cementitious matrix. The two reinforcements act at different scales and influence each other in the global structural response. Compared to classical limit state analysis, the

introduction of Fracture Mechanics concepts in the modeling of reinforced concrete members allows for determining ductile–brittle transitions, scale effects and contribution of fibers and, in general, nonlinear matrix tensile behavior. Moreover, crushing of the concrete is introduced in the model and an upper bound to the brittleness number is determined. When coupled to the results presented for the minimum reinforcement, this allows for defining a ductility domain. The ductility domain allows for designing the collapse mechanism for a beam in bending by simply evaluating its brittleness number. This extension to the model is here presented in the general case of simultaneous presence of fiber and steel bar reinforcement. It is however numerically tested in the case of conventional steel bar reinforcement due to limitations in the availability of experimental data.

**Acknowledgements** The present research was carried out with the financial support of the Italian Ministry of University and Scientific Research (MIUR) under the grant PRIN 2005 “Contact and Fracture Mechanics”.

## References

- Abdalla HM, Karihaloo BL (2003) Determination of size-independent specific fracture energy of concrete from three-point bend and wedge splitting tests. *Mag Concrete Res* 55:133–141
- Baluch MH, Azad AK, Ashmawi W (1992) Fracture mechanics application to reinforced concrete members in flexure. In: Carpinteri A (ed) *Applications of fracture mechanics to reinforced concrete*. Elsevier, London, pp 413–436
- Bosco C, Carpinteri A (1992a) Fracture mechanics evaluation of minimum reinforcement in concrete structures. In: Carpinteri A (ed) *Applications of fracture mechanics to reinforced concrete*. Elsevier, London, pp 347–377
- Bosco C, Carpinteri A (1992b) Softening and snap-through behavior of reinforced elements. *J Eng Mech (ASCE)* 118:1564–1577
- Bosco C, Carpinteri A (1995) Discontinuous constitutive response of brittle matrix fibrous composites. *J Mech Phys Solids* 43:261–274
- Bosco C, Carpinteri A, Debernardi PG (1990) Minimum reinforcement in high-strength concrete. *J Struct Eng (ASCE)* 116:427–437
- Bosco C, Carpinteri A, Debernardi PG (1992) Scale effect on plastic rotational capacity of r.c. beams. In: Bažant ZP (ed) *Fracture mechanics of concrete structures*. Elsevier, London, pp 735–740
- Carpinteri A (1981a) A fracture mechanics model for reinforced concrete collapse. In: *Proceedings of the I.A.B.S.E. colloquium on advanced mechanics of reinforced concrete*. Delft, pp 17–30

- Carpinteri A (1981b) Static and energetic fracture parameters for rocks and concrete. *Mater Struct* 14:151–162
- Carpinteri A (1984) Stability of fracturing process in RC beams. *J Struct Eng (ASCE)* 110:544–558
- Carpinteri A, Massabó R (1996) Bridged versus cohesive crack in the flexural behavior of brittle-matrix composites. *Int J Fract* 81:125–145
- Carpinteri A, Massabó R (1997a) Continuous vs discontinuous bridged-crack model for fiber-reinforced materials in flexure. *Int J Solids Struct* 34:2321–2338
- Carpinteri A, Massabó R (1997b) Reversal in failure scaling transition of fibrous composites. *J Eng Mech (ASCE)* 123:107–114
- Carpinteri A, Ferro G, Bosco C, Elkatieb M (1999) Scale effects and transitional failure phenomena of reinforced concrete beams in flexure. In: Carpinteri A (ed) *Minimum reinforcement in concrete members*, vol 24.ESIS Publications, Elsevier Science Ltd, pp 1–30
- Carpinteri A, Ferro G, Ventura G (2003) Size effects on flexural response of reinforced concrete elements with a nonlinear matrix. *Eng Fract Mech* 70:995–1013
- Ferro G (2002) Multilevel bridged crack model for high-performance concretes. *Theor Appl Fract Mech* 38:177–190
- Hawkins N, Hjørsetet K (1992) Minimum reinforcement requirement for concrete flexural members. In: Carpinteri A (ed) *Applications of fracture mechanics to reinforced concrete*. Elsevier, London, pp 37–412
- Hillerborg A (1990) Fracture mechanics concepts applied to moment capacity and rotational capacity of reinforced concrete beams. *Eng Fract Mech* 35:233–240
- Hillerborg A, Moder M, Petersson P (1976) Analysis of crack formation and crack growth in concrete by means of fracture mechanics and finite elements. *Cement Concrete Res* 6:773–782
- Jenq YS, Shah SP (1986) Crack propagation in fiber-reinforced concrete. *J Eng Mech (ASCE)* 112:19–34
- Karihaloo BL (1995) *Fracture mechanics and structural concrete*. Addison-Wesley, Longman
- Karihaloo BL, Wang J (2000) *Mechanics of fibre-reinforced cementitious composites*. *Comput Struct* 76:19–34
- Karihaloo BL, Abdalla HM, Imjai T (2003) A simple method for determining the true specific fracture energy of concrete. *Mag Concrete Res* 55:471–481
- Li VC, Wang Y, Backer S (1991) A micromechanical model of tension-softening and bridging toughening of short random fiber reinforced brittle matrix composites. *J Mech Phys Solids* 39:607–625
- Noghabai K (2000) Beams of fibrous concrete in shear and bending: experiment and model. *J Struct Eng (ASCE)* 126:243–251
- RILEM TC50 (1985) Determination of the fracture energy of mortar and concrete by means of three-point bend tests on notched beams. *Mater Struct* 18:287–290
- RILEM TC89 (1990) Determination of fracture parameters of plain concrete using three-point bend tests. *Mater Struct* 23:457–460
- Ruiz G (2001) Propagation of a cohesive crack crossing a reinforcement layer. *Int J Fract* 111:265–282
- Ruiz G, Elices M, Planas J (1998) Experimental study on fracture of reinforced concrete beams. *Mater Struct* 31:683–691
- Swamy RN, Al-Ta'an SA (1981) Deformation and ultimate strength in flexure of reinforced beams made with steel fiber concrete. *ACI J Proc* 5:395–405